Electrochimica Acta 298 (2019) 80–88

Contents lists available at ScienceDirect

Electrochimica Acta

journal homepage: www.elsevier.com/locate/electacta

Scanning electrochemical cell microscopy: A versatile method for highly localised corrosion related measurements on metal surfaces

Lewis C. Yule [a, b], Cameron L. Bentley [a], Geoff West [b], Barbara A. Shollock [b, c, **], Patrick R. Unwin [a, *]

[a] Department of Chemistry, University of Warwick, Coventry, CV4 7AL, UK
[b] Warwick Manufacturing Group, University of Warwick, Coventry, CV4 7AL, UK
[c] Kings College London, Strand, London, WC2R 2LS, UK

ARTICLE INFO

Article history:
Received 11 October 2018
Received in revised form
4 December 2018
Accepted 9 December 2018
Available online 11 December 2018

Keywords:
Corrosion
SECCM
Steel
Electrochemistry

ABSTRACT

The development of tools that can probe corrosion related phenomena at the (sub)microscale is recognized to be increasingly important in order to understand the surface structural factors (grain orientation, inclusions *etc.*) that control the (electro)chemical stability (corrosion susceptibility, pitting, passivity *etc.*) of metal surfaces. Herein we consider the application of scanning electrochemical cell microscopy (SECCM), a relatively new member of the electrochemical droplet cell (EDC) family, for corrosion research and demonstrate the power of this technique for resolving structure and activity at the (sub)microscale. Hundreds of spatially-resolved (2 μm droplet size) potentiodynamic polarization experiments have been carried out on the several hours timescale and correlated to complementary structural information from electron backscatter diffraction (EBSD) and energy dispersive x-ray spectroscopy (EDS) in order to determine the effect of grain orientation and inclusions on electrochemical processes at low carbon steel in neutral solution (10 mM KNO_3). Through this approach, it has been shown unequivocally that for the low index planes, anodic currents in the passive region (an indicator of corrosion susceptibility) are greatest on (101) planes compared to (100) and (111) planes. Furthermore, individual sub-micron MnS inclusions have been probed and shown to undergo active dissolution followed by rapid repassivation. This study demonstrates the high versatility of SECCM and the considerable potential of this technique for addressing structure-activity problems in corrosion and electromaterials science.

1. Introduction

The corrosion of metals and alloys is often caused by the establishment of local galvanic cells at surface heterogeneities when exposed to a corrosive environment (*e.g.*, an electrolyte solution). The (electro)chemical characteristics of these surface heterogeneities are not completely understood, largely due to the highly localised nature of the processes that occur [1]. As a consequence, the development of techniques that are able to extract spatially-resolved electrochemical information on the nanometer to micrometer length scales that can be correlated with complementary surface information are of great interest in order to resolve the relationship between structure (*e.g.*, metal grain orientation) and function (*e.g.*, corrosion resistance/susceptibility) [2,3].

In this study, we demonstrate how a simple micropipet imaging probe can be deployed in the scanning electrochemical cell microscopy (SECCM) [4] format to perform hundreds of spatially-resolved corrosion-relevant electrochemical measurements on the minutes to hours timescale so as to reveal the local electrochemical properties that are correlated with corresponding surface structure. SECCM operates on a similar principle as the electrochemical droplet cell (EDC) technique [5], whereby electrochemical measurements are confined to a small area of the surface with the use of a droplet formed at the end of an electrolyte filled microcapillary, equipped with auxiliary electrode(s). The EDC method allows for the direct, localised (spatially-resolved) investigation of (semi)conductive electrode substrates, and has previously been

* Corresponding author. Department of Chemistry, University of Warwick, Coventry, CV4 7AL, UK.
** Corresponding author. Kings College London, Strand, London, WC2R 2LS, UK.
E-mail addresses: nms_ea@kcl.ac.uk (B.A. Shollock), p.r.unwin@warwick.ac.uk (P.R. Unwin).

https://doi.org/10.1016/j.electacta.2018.12.054

used to study microscale corrosion processes on metals such as 304 stainless steel [6–8], duplex stainless steel [9–11] and aluminium [12,13]. Herein, we show that SECCM possesses all of the advantages of the EDC technique for corrosion research, while achieving significant improvements in terms of speed, resolution and reproducibility, through the use of a simplified probe design and advanced positioning technology.

SECCM belongs to the scanning electrochemical probe microscopy (SEPM) family of techniques, among which scanning electrochemical microscopy (SECM) is the most used [3,14,15]. SECM has previously been applied to the study of corrosion processes at materials including, carbon steel [16], stainless steel [17,18], pure iron [19,20] and titanium [21]. Nevertheless, despite its popularity, SECM contrasts with EDC methods in that it probes electrochemical processes (*e.g.*, corrosion) *indirectly* by monitoring the concentrations and fluxes of reactant, product or intermediates (*e.g.*, oxygen, protons or metal ions) by electrochemistry at the probe (tip), and thus only chemical species can be detected amperometrically or, more rarely, potentiometrically. Furthermore, the tip response must remain stable for the entire duration of a scan.

SECCM enables direct voltammetric-amperometric measurements at a series of targeted positions of a sample surface [22–25] and has previously been applied to resolve the relationship between structure and activity in a wide range of electrochemical processes at a diversity of electrode materials (*e.g.*, sp^2 carbon materials [26], molybdenum disulfide [27], iron nickel sulphide catalysts [28], and metallic nanoparticles [23,24]), but has not yet been employed to study corrosion related phenomena. Here, we report the first use of SECCM, operated in voltammetric mode, for probing spatially-resolved corrosion properties, illustrated through the study of polycrystalline low carbon steel in neutral (10 mM KNO_3) media. Used ubiquitously in construction, the corrosion properties (*i.e.*, susceptibility/resistance) of low carbon steel are known to be significantly influenced by chemical composition (*e.g.*, alloying elements and inclusions) and/or microstructure (*e.g.*, crystallographic orientation and/or phase) [29,30]. The structural/compositional dependence is shown unequivocally in this work, where differences in the corrosion susceptibility of the low-index (100), (101) and (111) grains is elucidated from spatially-resolved voltammetric measurements and the direct electrochemical detection and characterisation of sub-micron sized manganese sulphide inclusions is demonstrated.

2. Experimental

Chemical reagents and electrode materials. The low carbon steel sample (composition detailed in Table 1) was provided by Tata Steel, Research and Development (U.K.). In order to prepare the sample for measurement, the steel sheet was sectioned using an abrasive cutter to give a sample of size (approx.) 5 × 21 × (thickness) 2 mm, which was subsequently mounted in a carbon-based conductive mount using a Buehler SimpliMet 3000 Mounting Press (Buehler, U.S.A.). After mounting, the sample was polished on a polishing cloth (Buehler Trident) using (successively) 9 μm, 3 μm and 1 μm polishing suspensions (Buehler MetaDi Supreme Suspension). The final polishing step was carried out on a polishing cloth (Buehler MicroCloth) using 0.05 μm alumina suspension (MasterPrep Sol-gel, Buehler). After polishing, the sample was washed in acetone, soapy water and then thoroughly in copious amounts of deionized water, before being gently blown dry. Electrical connection to the sample was made with a copper wire connected to the outside of the conductive mount with carbon tape.

Table 1
Chemical composition of the low carbon steel determined using energy dispersive X-ray spectroscopy.

%	C	Mn	Si	Cr	Al	P	S	Cu
Low Carbon Steel	0.05	0.3	<0.03	0.06	0.03	<0.02	<0.02	0.04

Potassium nitrate (KNO_3, Sigma-Aldrich), potassium chloride (KCl, Sigma-Aldrich) and dichlorodimethylsilane [$Si(CH_3)_2Cl_2$, Acros Organics, ≥99%] were used as supplied. All solutions were prepared with ultra-pure deionized water (Integra HP, Purite, U.K.), which had a resistivity of 18.2 MΩ cm at 25 °C.

Surface characterisation. All surface characterisation was carried out with a Zeiss SIGMA FE-SEM (Zeiss, Germany), using an X-Max 50 mm^2 energy-dispersive X-ray spectroscopy (EDS) detector (Oxford Instruments, U.K.) and an Nordlys EBSD detector (Oxford Instruments, U.K.). SEM images and EDS data were collected at 5 keV, whereas EBSD images were collected at 20 keV, with the sample tilted at 70° to the detector. Following EBSD characterisation, grains that were chosen for the present study were either on or close to the low index orientations, (100), (101) and (111). The criterion for plane selection set in this study was 10° deviation from the desired orientation.

Macroscale polarization measurements. A Teflon cylinder with an inner diameter of 2 mm was attached to the low carbon steel surface with silicone adhesive. A commercial Ag/AgCl reference electrode (3.4 M KCl, eDAQ, Australia) and a platinum counter electrode were inserted into the cylinder which was filled with 10 mM KNO_3 solution. The measurement was carried out at a sweep rate of 80 mV s^{-1} using a CHI400 potentiostat (CH Instruments Inc., U.S.A).

SECCM probe fabrication. The SECCM micropipet probes were pulled from borosilicate theta capillaries (TG 150-10, Harvard Part No. 30-0114, Harvard Apparatus, U.S.A.) using a P-2000 laser puller (Sutter Instruments, USA). The size (overall diameter) of the opening at the end of the pipet was approximately 2 μm, as determined by FE-SEM. To aid meniscus (droplet) confinement, the outer walls of the pulled pipet tip were silanized with dichlorodimethylsilane, as previously described [4]. This was achieved by submerging the tip in $Si(CH_3)_2Cl_2$ with argon flowing from the bottom of the probe at a pressure of 6 bar (this prevented the silane from entering the tip during immersion). During this process, the organosilane becomes covalently attached to the glass surface, to produce a robust and resistant hydrophobic coating on the outer wall of the micropipette that does not contaminate the sample surface or need to be reapplied during the scan. The droplet (meniscus) cell was formed at the end of the pipet by filling each channel of the probe with 10 mM KNO_3 solution. A small amount of silicone oil (Fluka Analytical) was inserted on top of the KNO_3 solution to reduce the evaporation during prolonged SECCM scanning experiments, as previously reported [27]. After filling, Ag/AgCl quasi reference counter electrodes (QRCEs) were inserted into each channel of the dual barrelled probe. The Ag/AgCl QRCEs were prepared by anodizing 0.125 mm diameter annealed silver wire (Goodfellow, U.K., 99.99%) in a saturated KCl solution, and have previously been shown to possess long-term stability and not to contaminate the surface investigated in a variety of electrolyte solutions [31]. The Ag/AgCl QRCE has a potential of *ca.* 0.25 V vs. saturated calomel electrode (measured potentiometrically) when immersed in 10 mM KNO_3.

SECCM set up. The SECCM set up (shown schematically in Fig. 1a) has been reported in detail previously [4,22]. Briefly, the micropipet probe was mounted on a *z*-piezoelectric positioner (P-753.3CD, PhysikInstrumente, Germany) to which a periodic oscillation (perpendicular to the sample) was applied (250 nm peak-to-peak amplitude at a frequency of 286 Hz) by an *ac* signal generated

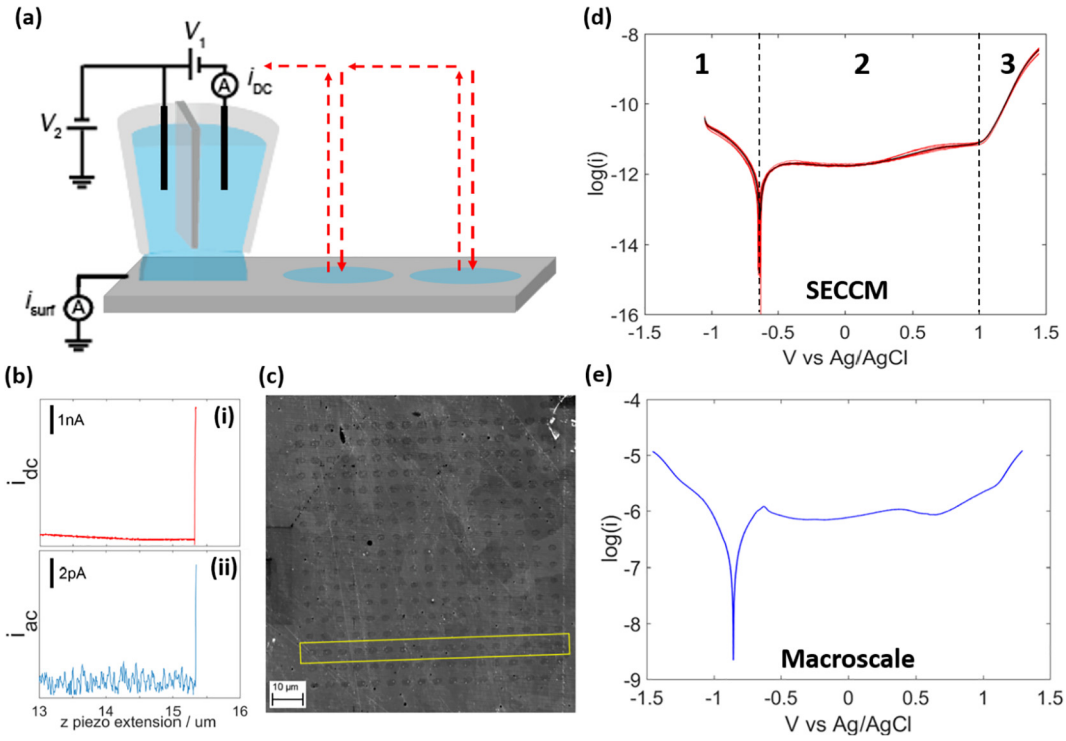

Fig. 1. **(a)** Schematic showing the voltammetric hopping-mode SECCM protocol employed to make spatially-resolved potentiodynamic polarization measurements at a sample surface. The arrows indicate the path of probe across the surface. **(b)** Plots of the (i) *dc* and (ii) *ac* ionic current versus *z*-position as the micropipet probe is approached towards a low carbon steel surface. The surface was detected at an extension of 15.34 µm. **(c)** FE-SEM image of a 17 × 17 matrix of droplet 'footprints' on a low carbon steel surface, left after making spatially-resolved potentiodynamic polarization measurements using the SECCM setup outlined in (a). **(d)** Individual (red) and averaged (black) Tafel plots resulting from the row of droplet footprints highlighted by the yellow box in (c), obtained in a 10 mM KNO_3 solution at a sweep rate of 80 mV s^{-1}. The three 'regions' indicated in (d) correspond to: (1) cathodic, (2) passive and (3) transpassive behaviour of the metal electrode surface. **(e)** Tafel plot taken from a macroscopic polarization measurement of the low carbon steel in 10 mM KNO_3 at a sweep rate of 80 mV s^{-1}.

by a lock-in amplifier (SR830, Stanford Research Systems, U.S.A.). A bias potential (V_1) of +0.1 V was applied between the QRCEs in order to generate an ion conductance current (i_{dc}) across the liquid meniscus formed at the end of the probe, which was used as a feedback signal during positioning of the micropipet probe relative to the substrate (steel) surface (*e.g.*, see Fig. 1b–i below). The micropipet was positioned above the low carbon steel surface using micropositioners for coarse movement and an *xy*-piezoelectric positioner (P-621.2CD, PhysikInstrumente) for fine movement laterally (parallel to the sample).

During operation, the probe was approached to the substrate surface at a constant velocity (*ca.* 0.2 µm/s here) applied to the z-piezoelectric positioners, and once contact between the droplet (meniscus) cell and the surface had been established (the pipet probe itself did not make contact with the surface), the ion conductance current showed a periodic modulation (*ac* component, i_{ac}) at the same frequency of oscillation (measured with the same lock-in amplifier highlighted above) due to reversible deformation of the droplet [32]. The magnitude of i_{ac} informs on the status of the droplet (*e.g.*, see Fig. 1b–ii). An i_{ac} set point of 6 pA was used as the feedback signal herein and electrochemistry was performed within the area contacted by the meniscus cell. A substrate voltage of V_2 was applied to one of the QRCEs to control the working electrode (*e.g.*, low carbon steel) potential (E_S), where $E_S = -(V_1/2 + V_2)$ [32], and the working electrode current (i_{surf}) was measured. The size of the confined area (*i.e.*, working electrode area) was determined after each set of measurements by FE-SEM imaging of the droplet "footprint" residue, as discussed in detail below.

Electrochemical measurements at the low carbon steel (working electrode) were made using a cyclic voltammetric "hopping" regime, as described previously [22,27,33]. In essence, the micropipet probe made a series of measurements by performing potentiodynamic polarization at predefined locations in a grid. The hopping distance (*i.e.*, spatial resolution) between each pixel was 5 µm to avoid overlap of the probed areas.

The entire SECCM apparatus was supported on an optical table (Thorlabs, U.S.A.) and shielded with a Faraday cage equipped with heat sinks and vacuum panels to minimise noise and variations in temperature (temperature of measurements *ca.* 21 °C). The QRCE potentials were controlled (with respect to ground) with a home-built bipotentiostat and the low carbon steel substrate (working electrode, common ground) current was measured using a home-built electrometer. Each data point in the voltammetric measurements was taken as an average of 1025 samples recorded at 10 µs intervals (*i.e.*, approximately every 10 ms). The scan rates used in this study were 40, 50 and 80 mVs^{-1} which resulted in data points being acquired every 0.4, 0.5 and 0.8 mV. Data acquisition and fine control of all instrumentation was achieved using an FPGA card (PCIe-7852R) controlled by a LabVIEW 2016 (National Instruments, U.S.A.) interface running the Warwick Electrochemical Scanning Probe Microscopy (WEC-SPM, www.warwick.ac.uk/electrochemistry) software. Data treatment and analysis was carried out using the Matlab R2015b (8.6.0.267246, Mathworks, U.S.A.) and OriginPro 2016 64bit (b9.3.226, OriginLab, U.S.A.) software packages. The standard error of the average potentiodynamic polarization curves was calculated by dividing the standard deviation by the square root of the number of data points.

3. Results and discussion

SECCM: operational principles and practical considerations. In a recent comprehensive review [2], droplet cell based-techniques (*i.e.*, the EDC technique) were considered to have several serious limitations in spatially-resolved corrosion research. Our intention here is to show that these limitations are readily overcome with SECCM, positioning it as a powerful technique for spatially-resolved corrosion-related measurements. A first issue raised is that the probe dimensions (*i.e.*, micro-capillary size), which ultimately determines the spatial resolution of the technique, is limited by the current resolution of the potentiostat (*i.e.*, small probes give rise to currents that are too small to measure accurately) [34]. This is not an issue for the SECCM set up used herein, as demonstrated by previous studies by our group [35–39], where currents as low as a few fA were measured with excellent signal-to-noise and reasonable time resolution, noting the well-known bandwidth-current magnitude trade off [40].

A second issue concerns the complexity of fabricating the droplet cell micro-probes. In conventional micro-cell experiments, the microcapillary probes are fabricated from pulled glass pipets, which are ground and polished until the required size is achieved, before the application of a silicone rubber gasket on the tip [5,6]. This is a somewhat laborious process. In addition, although the silicone rubber gaskets reportedly improve the versatility and reliability of the conventional micro-cell technique by ensuring electrolyte confinement and contact with the surface [5,6], the inconsistent quality of the probe-surface contact can lead to a risk of crevice corrosion in the scanning area, thus drastically affecting the electrochemical response [41]. In addition, probe-surface contact is traditionally made manually using a microscope to judge when the gasket has made a seal with the surface [2], which is both time-consuming and relatively irreproducible, as the contact may vary from point-to-point.

By contrast, the micropipet (or nanopipet [23,24]) probes in SECCM can be fabricated quickly and reproducibly using a laser puller, with no need to apply a silicone rubber gasket [4,42]. In SECCM, consistent droplet-cell surface contact is achieved by silanizing the outer wall of the probe (detailed in the Experimental Section), to make it hydrophobic, which aids in droplet confinement during meniscus surface contact [4]. As highlighted above, the ion conductance current between the QRCEs in the dual channel probe is sensitive to the size and shape of the meniscus between the end of the pipet and surface, and a set point value of the *ac* conductance current, i_{ac} (*e.g.*, when the droplet initially makes contact with the surface, see Fig. 1b) ensures consistent meniscus contact, without the need for a gasket. Thus, the approach and contact of the meniscus with the steel surface is automated and precisely controlled. This is a key advantage of the technique, enabling large numbers of surface measurements to be made in a reasonable time (*vide infra*) and thus making the measurements more statistically sound than with other droplet cell methods (*e.g.*, conventional EDC).

A third issue is the possibility of high ohmic (*iR*) resistance between the working and counter-reference electrodes [43,44]. A significant ohmic drop is expected when large currents are passed between the working and counter electrodes with capillaries on the order of 100 μm [43]. In SECCM, the ion current between the two chambers (i_{dc}, see Fig. 1b) reveals the pipet resistance, which is *ca.* 50 MΩ herein [$R = E/i_{dc} = +0.1\ V/(2 \times 10^{-9}\ A) = 5 \times 10^{7}\ \Omega$]. Thus, by setting a limit of 5 mV on the ohmic drop, this means that surface currents up to *ca.* 100 pA are essentially immune to ohmic effects, *i.e.*, only in the transpassive region (*region 4, vide infra*) of the Tafel plots in Fig. 1d is ohmic drop a consideration. Another risk of biasing the potential to the transpassive region is the effect of extensive corrosion products on the stability of the probe (QRCEs and electrolyte) between scanning points. To avoid this, previous studies [45] have restricted the applied potential to values outside of the transpassive region, which is the approach that has mainly been applied herein.

Finally, the potentiodynamic sweep rate for the polarization experiments is a critically important consideration. Traditionally, the potentiodynamic sweep rates employed in corrosion research are extremely low (<1 mV s^{-1}), which facilitates the straightforward calculation of the corrosion potential (E_{corr},) and corrosion current (i_{corr}), taken indicators of bulk corrosion susceptibility/resistance [46,47]. By contrast, high potentiodynamic sweep rates are preferable in the micro-droplet format in order to minimise perturbation to the sample surface and solution at the end of the tip and to avoid tip blocking [12], as well as to reduce the time taken for the electrochemical map to be produced. In addition to changing the timescale of the experiment, current from nonfaradaic processes (i_{nf}) such as double layer charging and stray capacitance becomes more prevalent at high sweep rates, evident in the current-potential (*i-E*) plots in Fig. 2a, which show voltammetric segments recorded between 0.15 and −1.05 V vs Ag/AgCl QRCE at scan rates between 0.01 Vs^{-1} and 0.5 Vs^{-1}. As shown in Fig. 2b, the sweep rate has a significant effect on i_{nf} distortion of the logarithmic Tafel plots that gives rise to an apparently sweep rate-dependent E_{corr} and i_{corr}, as noted previously [46]. For this reason these parameters will not be considered as indicators of corrosion resistance/susceptibility herein. Rather, we are able to draw on other parameters from the voltammetric response.

As highlighted above in the Experimental Section, for this work, a voltammetric hopping mode regime [22,27,33] was used, whereby a potentiodynamic polarization measurement was made at a series of spatially-resolved 'pixels' on the substrate surface. Returning to Fig. 1, representative SECCM potentiodynamic polarization curves (plotted in Tafel form), on low carbon steel are very reproducible (Fig. 1d) which shows Tafel plots obtained from the row (17 sites) of a scan (indicated in Fig. 1c), alongside the average plot from this row.

The data in Fig. 1d reflect the expectations from the Pourbaix diagram for an iron electrode in neutral solution [48]. The potential sweep initially starts in the cathodic region (*region 1* in Fig. 1d), where hydroxide (OH^-) generation dominates, arising from a combination of the oxygen reduction reaction (ORR) and the hydrogen evolution reaction (HER):

$$O_2 + 2H_2O + 4e^- \rightarrow 4OH^- \quad (1)$$

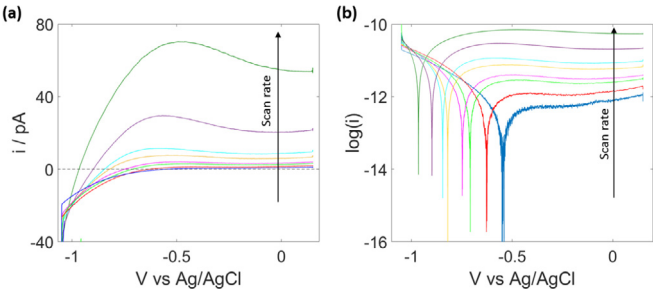

Fig. 2. Potentiodynamic polarization experiments carried out at adjacent sites on a low carbon steel surface in 10 mM KNO_3 with a 2 μm diameter micropipet probe at sweep rates of (top to bottom) 0.5, 0.2, 0.1, 0.08, 0.05, 0.04, 0.02 and 0.01 V s^{-1}. The data are presented as **(a)** *i-E* plots and **(b)** corresponding Tafel plots. The apparent shift in E_{corr} is caused by the increased contribution of nonfaradaic (charging) current to the total measured current with increasing sweep rate (see text).

$$2H_2O + 2e^- \rightarrow H_2 + 2OH^- \quad (2)$$

Note that in the SECCM configuration, there is an enhanced flux of O_2 across the air-water-electrode three phase boundary [49]. In addition to the ORR, any existing passive film on the steel surface is expected to be at least partially reduced in the cathodic region of the Tafel plot (*i.e.*, *region 1* in Fig. 1d).

As the system passes through E_{corr} an active region is not observed, and the steel essentially passivates instantly on the timescale of these measurements. The production of ferrous and ferric hydroxide is expected [50], for example via the reactions shown in eqs. (3) and (4):

$$Fe + 2H_2O \rightarrow Fe(OH)_2 + 2H^+ + 2e^- \quad (3)$$

$$Fe^{2+} + 3OH^- \rightarrow Fe(OH)_3 + e^- \quad (4)$$

where OH^- arises from the ORR and HER, as noted above (Eqs. (1) and (2)). *Region 2* is the passive region, where $Fe(OH)_2$ and $Fe(OH)_3$ are further oxidised to form a (semi) protective passive film on the surface [50], effectively suppressing corrosion throughout this potential range:

$$2Fe(OH)_2 \rightarrow Fe_2O_3 + H_2O + 2H^+ + 2e^- \quad (5)$$

$$3Fe(OH)_3 \rightarrow Fe_3O_4 + H_2O + 2H^+ + 2e^- \quad (6)$$

Region 3 is the transpassive region, where the oxygen evolution (Eq. (7)) or the complete breakdown of the passive layer formed in *region 3* results in bulk dissolution of the underlying metal.

$$2H_2O \rightarrow O_2 + 4H^+ + 4e^- \quad (7)$$

By comparing the results collected using SECCM (Fig. 1d) with those collected at the macroscale (Fig. 1e) it is clear the corrosion potential is shifted more positive when using SECCM. As previously mentioned [49], the droplet cell configuration enables a high flux of oxygen (across the meniscus/air interface) compared to the "bulk solution" conditions of the macroscopic experiment. Therefore, the ORR is enhanced in SECCM experiments. By assuming the anodic branch for both SECCM and macroscopic experiments behaves similarly, higher rates of cathodic reactions results in the positive shift of the corrosion potential in accordance with mixed potential theory [51]. In addition, in the macroscale Tafel plot a small oxidation peak arises following the corrosion potential which does not appear in the SECCM Tafel plot. This is because the enhanced oxygen reduction in SECCM limits the anodic currents, thus subduing this peak, as the current, i, is a sum of the cathodic, i_c, and anodic processes, i_a, (Eq. (8)).

$$i = i_c + i_a \quad (8)$$

Crystallographic orientation and corrosion susceptibility in low carbon steel. We now explore the relationship between electrochemical behaviour (*e.g.*, corrosion resistance/susceptibility) and crystallographic (grain) orientation to highlight a major capability of SECCM when spatially-resolved voltammetric data are combined with EBSD data of the same area of the surface (correlated or co-location electrochemical multi-microscopy). Many studies have attempted to explain the link between crystallographic orientation and the electrochemical behaviour of metals, as exemplified by studies of iron [52–55], pearlitic steel [56], FeAlCr ferritic steel [57], 316L stainless steel [58] and aluminium [59]. However, although the crystallographic orientation affects the electrochemical behaviour of metal surfaces, to the best of our knowledge, there is no clear trends, nor are there consistent explanations for the differences in electrochemical behaviour observed between the grains.

SECCM was used to electrochemically map an area on a low carbon steel sample, as shown in Figure 3a. Each droplet 'footprint' in the image corresponds to an individual potentiodynamic polarization experiment carried out in 10 mM KNO_3 at a sweep rate of 50 mV s^{-1} (*e.g.*, see Fig. 1c). The 256 individual potentiodynamic polarization experiments were made over a total scan time of 6 h, and from Fig. 3a it is clear that the geometry of the droplet cell does not change on this timescale (*i.e.*, the droplet 'footprint' size is reproducible). The same area of the steel surface was subsequently mapped using EBSD, as shown in Fig. 3b. Evidently, a significant number potentiodynamic polarization experiments were made on each of the (100), (110) or (111) orientated grains (and other orientations, Fig. 3c). This 'pseudo single crystal' approach [60] of the SECCM technique allows multiple crystallographic orientations on a polycrystalline sample to be independently interrogated in a single experiment.

The raw *i-E* data were extracted from each point shown in

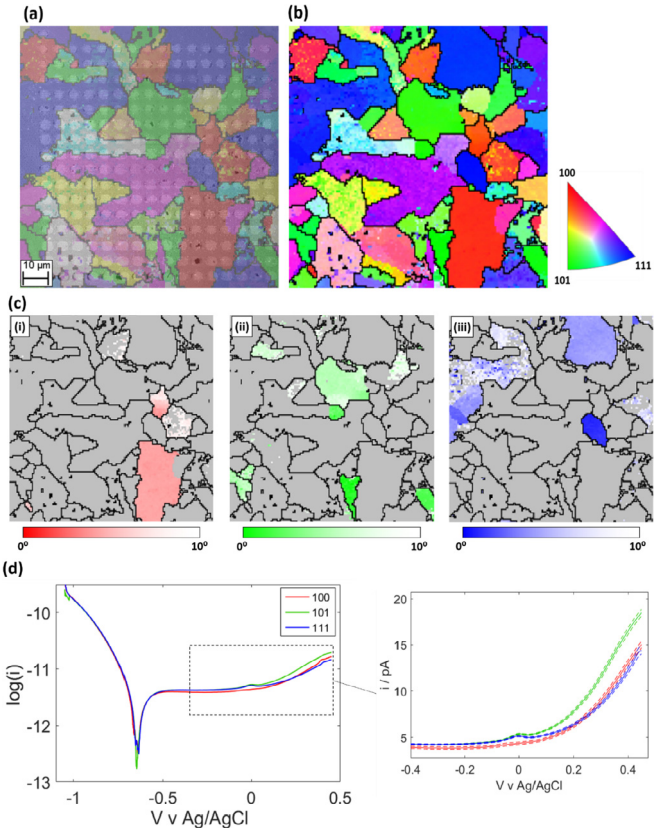

Fig. 3. **(a)** SEM image with the EBSD map superimposed and **(b)** the corresponding EBSD map of the area of the low carbon steel surface that was characterized with SECCM. The droplet 'footprints' remaining after each of the individual 256 potentiodynamic polarization experiments are clearly visible in (a). **(c)** Grains deemed close enough to the low index planes are shown in **(i)**, **(ii)** and **(iii)** for (100), (101) and (111), respectively. **(d)** Representative Tafel plots obtained on the (100) (red trace), (101) (green trace) and (111) (blue trace) grains on the area of the low carbon steel surface shown in (a) and (b). The plots were obtained by averaging the *i-E* data collected during spatially-resolved potentiodynamic polarization measurements made with SECCM. 15, 12 and 26 individual measurements were averaged on the (100), (101) and (111) grains, respectively. The polarization experiments were carried out in 10 mM KNO_3 at a potentiodynamic sweep rate of 50 mV s^{-1} using a micropipet probe with a diameter of 2 µm. The highlighted section is of the potential region spanning −0.4 to +0.45 V vs. Ag/AgCl, which is shown magnified in the *i-E* plot. The dashed lines included above and below the traces represents the standard error of the data.

Fig. 3a, assigned to a dominant grain (the grains that were chosen and considered suitable for study are shown in Fig. 3c), and then averaged to give the Tafel plots shown in Fig. 3d. The results are representative because there are 15, 12 and 26 individual measurements on the (100), (101) and (111) grains, respectively. The cathodic branch of the Tafel plots, corresponding to the ORR, HER and/or reduction of the pre-existing passive film on the low carbon steel surface (discussed above), are very similar for each of the grains, indicating that these reactions do not have a strong surface-orientation-dependence on this surface, under these conditions. In the passive region and moving in the anodic direction, the current is comparable on each of the grains up to an applied potential of approximately 0 V vs. Ag/AgCl QRCE, where upon the (101) grain gives rise to larger anodic currents than the (100) and (111) grains. Considering this potential region corresponds to passive film formation/growth (*e.g.*, see Eqs. (5) and (6)), these results suggest that the passive film formed on the (101) grain is less effective at preventing anodic dissolution than that formed on the (100) or (111) grains. Supporting this deduction is an additional electrochemical (SECCM) scan, EBSD and FE-SEM images for the same low carbon steel sample in a different area, with the results summarised in Fig. 4. Comparing the FE-SEM image in Fig. 4a, with the EBSD maps

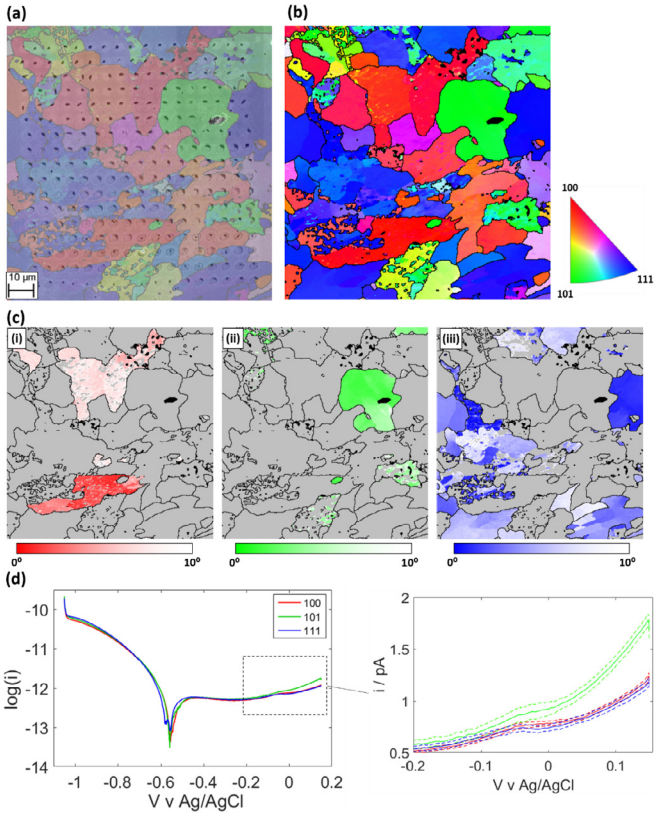

Fig. 4. **(a)** SEM image with the EBSD map superimposed and **(b)** corresponding EBSD map of the area of the low carbon steel surface that was characterized with SECCM. **(c)** Grains deemed close enough to the low index planes are shown in **(i)**, **(ii)** and **(iii)** for (100), (101) and (111), respectively. **(d)** Representative Tafel plots obtained on the (100) (red trace), (101) (green trace) and (111) (blue trace) grains on the area of the low carbon steel surface shown in **(a)** and **(b)**. The data were obtained by averaging the *i-E* data collected during spatially-resolved potentiodynamic polarization measurements made with SECCM. 41, 19 and 38 individual measurements were averaged on the (100), (101) and (111) grains, respectively. The polarization experiments were carried out in 10 mM KNO_3 at a sweep rate of 40 mV s^{-1} using a micropipet probe with a diameter of 2 µm. The highlighted section is of the potential region spanning −0.2 to +0.15 V vs. Ag/AgCl, which is shown magnified in the *i-E* plot. The dashed lines included above and below the traces represents the standard error of the data.

in Fig. 4b to extract the averaged Tafel plots in Fig. 4d, it is clear that the (101) grain gives rise to higher anodic currents than the (100) or (111) grains in the passive region.

What is also noticeable is that a small peak arises at approximately 0 V vs Ag/AgCl on Fig. 3d on the (101) and (111) grains, but interestingly not on the (100) grains. Given the potential of this peak, we considered the deposition/stripping of Ag(0) arising from the Ag/AgCl QRCE as a possible origin, however if this were the case, this peak would be seen on all grains, and furthermore such problems are easily avoided with care [31], as taken in this paper. Therefore we can rule this out as an explanation. Furthermore, detailed analysis of the voltammograms indicated that this peak occurred in all measurements on (101) and (111) grains but not once on the (100) grains. The amount of charge passed under this peak corresponds to ca. 1% of a monolayer over the scanned area which indicates this is a very subtle process. It is therefore very difficult to speculate on the origin of this peak, although this finding does show the capability of SECCM to detect these very subtle grain dependent electrochemical processes.

In previous studies [52], differences between the relative corrosion susceptibility of the grains have been attributed to the geometry of each grain surface, particularly the surface atom density. The planar packing factor increases in the order (111) < (100) < (101) (with values 0.340, 0.589 and 0.833, respectively) for the body-centred cubic (BCC) crystal system considered herein. It appears that the higher the density of atoms exposed to the solution (*i.e.*, present at the surface plane), the greater the chance of anodic oxidation, resulting in greater corrosion susceptibility for the densely packed (101) grain compared to the (100) or (111) grains. This is consistent with previous studies [54,61] that observed the (101) plane on iron to exhibit higher anodic dissolution currents than the (100) plane. This was attributed due to the higher atomic density at the surface of the exposed (101) grains. However, there is also an argument that this difference is due to the nature of the passive film formed on the (101) and (100) grains, as suggested above. It has been reported [62] that a thicker (and therefore perhaps more protective) passive film forms on (100) than (101) grains on iron, which could also be responsible for the increased anodic currents measured on (101) grains.

It is important to note that although the influence of the planar packing factor can be used to explain why there is an increased response from (101) planes in the passive region, it does not explain why little to no difference is observed in the response from the (100) and (111) planes. One reason for this could be that the difference is too subtle to detect, although more likely is that the density of atoms at the surface is not the only influence on the corrosion behaviour of different crystal planes. As noted before, previous studies [52,53,57,59] have struggled to maintain consistent explanations for this variation between grains suggesting the problem is more complex and involves other factors than just surface atom density. In a recent review, a number of surface properties affecting the corrosion of carbon steel are discussed in detail [63].

Detecting and probing electrochemistry at MnS inclusions in low carbon steel. MnS inclusions are well-known onset sites for localised (pitting) corrosion in stainless steel and steel alloys [64,65]. As shown in Fig. 5, the low carbon steel used herein contains MnS inclusions of sizes ranging from 200 nm to 1 µm. It follows that when performing SECCM mapping on an area of this low carbon steel sample, some of the probed areas (droplet footprints) will contain a MnS inclusion.

Potentiodynamic polarization curves obtained in the SECCM format, in areas containing MnS inclusions are shown in Fig. 6. In each plot, three Tafel curves are shown, corresponding to the site containing the inclusion (labelled 2 in Fig. 6a) and two adjacent

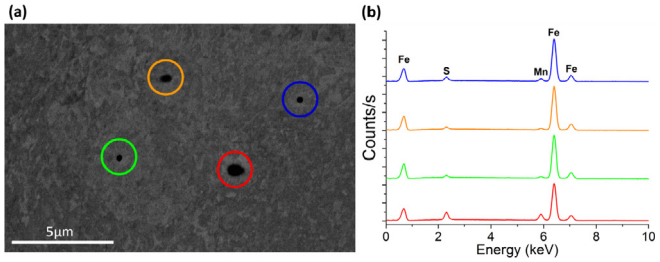

Fig. 5. (**a**) SEM image of MnS inclusions (indicated by coloured circles) on a low carbon steel surface. **(b)** Energy dispersive X-ray spectroscopy (EDS) responses of each of the inclusions, with the colours corresponding to the inclusions highlighted in **(a)**.

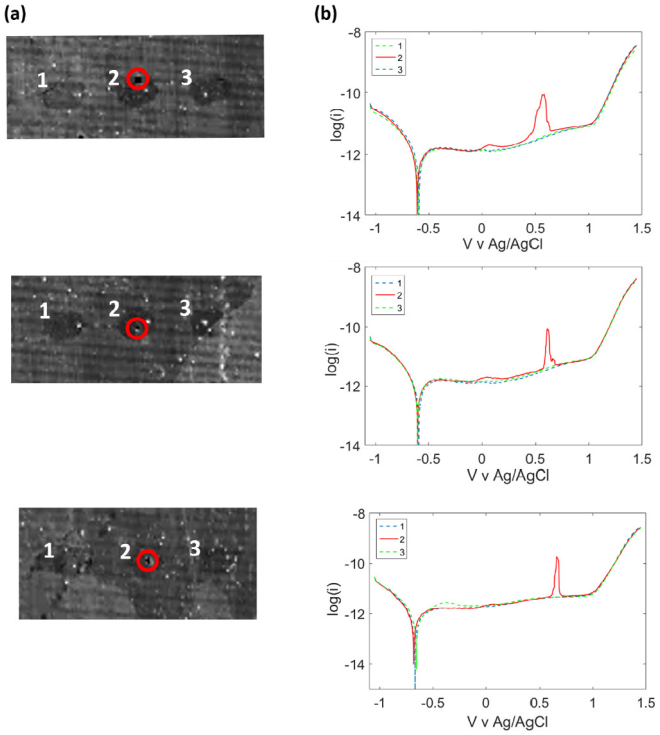

Fig. 6. **(a)** SEM images of adjacent droplet footprints with (2) and without (1 and 3) an MnS inclusion (indicated by a red circle). **(b)** Tafel plots obtained at the corresponding points labelled in (a). The potentiodynamic polarization experiments were performed in the SECCM format (probe diameter = 2 μm) on low carbon steel in 10 mM KNO_3 at a sweep rate of 80 mV s^{-1}.

sites containing no inclusions (labelled 1 and 3 in Fig. 6a). The Tafel plots in Fig. 6b, obtained at the inclusion sites show an abrupt increase in anodic current in the passive region at a potential of approximately 600 mV vs. Ag/AgCl, which immediately returns to the original passive value, giving rise to an anodic current 'spike'. This 'spike' in the current is consistent with findings of Webb et al. [66], who used a 100 μm microcapillary to land on rather large MnS inclusions in 304 stainless steel, and found similar current-potential behaviour on the same inclusions.

Comparing the data in Fig. 6 to the findings of Webb et al. [66], it is clear that the current 'spikes' are attributable to the dissolution and immediate re-passivation of the MnS inclusion within the probed droplet cell area. This is also consistent with the fact that the inclusion is still visible within the probed area after the polarization experiment (the inclusions are labelled in Fig. 6a). These results highlight the excellent spatial resolution achievable with SECCM, in detecting inclusions that are on the sub-micron scale. It is interesting to note that the cathodic branch of the Tafel plots is not significantly affected by the presence of the MnS inclusions (Fig. 6b). Although this suggests that MnS does not catalyse the ORR/HER under these conditions, it needs to be noted that the inclusions only comprise a very small portion of the probed area (droplet 'footprints', estimated to be <10% from Fig. 6a). For this reason, in order to be detectable with the micron-sized probe used herein, the sub-micron MnS inclusions would need to possess very high activity relative to the steel surface, as is seen in the anodic case (*i.e.*, the MnS is active, whereas the steel is passive), but not necessarily the cathodic case (*i.e.*, both the MnS and steel are active). Future work will make use of smaller probes, allowing the electrochemical activity of sub-micron surface features, such as inclusions and grain boundaries to be investigated directly.

4. Conclusions

Scanning electrochemical cell microscopy (SECCM) has been used to probe local electrochemical phenomena related to corrosion processes at the microscale. The working principles of the technique have been demonstrated and the advantages compared to earlier electrochemical droplet cells (EDCs) have been outlined. The applicability of SECCM to corrosion-related research has been demonstrated through studies of a body centred cubic (BCC) structured polycrystalline low carbon steel in aqueous electrolyte media (10 mM KNO_3). Through combination of spatially-resolved electrochemical information from SECCM with complementary structural information from EBSD in a *correlative multi-microscopy approach*, it was shown unequivocally that for the low index planes, anodic currents in the passive region (*i.e.*, corrosion susceptibility) were greatest on (101) planes compared to (100) and (111) planes. Thus, the more densely packed (101) was most susceptible to anodic oxidation under these neutral pH conditions. In future studies, electrochemical data will be considered across the entire spectrum of crystallographic orientations, rather than just the low index planes, in order to gain a holistic view of the structural factors controlling corrosion susceptibility/resistance at metal surfaces.

SECCM was additionally applied to study the electrochemical behaviour of individual sub-micron MnS inclusions embedded in the low carbon steel surface, which were shown to give rise to large anodic current 'spikes' in the passive region, attributable to the electrochemical dissolution and subsequent repassivation of the inclusion. This aspect of the study highlights the ability of SECCM to probe sub-micron to nanoscale surface features and bodes well for future investigations of inclusions and grain boundaries.

This study has further demonstrated the wide applicability of SECCM in materials research. The technique was successfully applied to perform hundreds of μm-resolved corrosion measurements on the several hours timescale. Recent work [23,24] has demonstrated further improvements of SECCM in terms of speed and resolution, with thousands of nm-resolved measurements now possible on the tens of minutes timescale. Moving forward, we believe that SECCM will have an important role to play in corrosion science. Understanding structure-activity is highly important in corrosion science, and as demonstrated by this initial study, high-resolution correlation of electrochemical data with the underlying structure and properties of the surface will enhance knowledge of the electrochemical processes that drive corrosion.

Acknowledgements

This work was supported by an iCASE award to L.Y. from the Engineering and Physical Sciences Research Council and Tata Steel Research and Development. C.L.B. acknowledges support from the

European Union's Horizon 2020 research and innovation programme under the Marie Skłodowska-Curie grant agreement No. 702048 (NEIL). P.R.U. gratefully acknowledges support from a Royal Society Wolfson Research Merit Award. The authors also acknowledge Dr Digvijay Thakur from Tata Steel Research and Development.

References

[1] G.S. Frankel, N. Sridhar, Understanding localized corrosion, Mater. Today 11 (2008) 38–44, https://doi.org/10.1016/S1369-7021(08)70206-2.
[2] F. Andreatta, L. Fedrizzi, The use of the electrochemical micro-cell for the investigation of corrosion phenomena, Electrochim. Acta 203 (2016) 337–349, https://doi.org/10.1016/j.electacta.2016.01.099.
[3] N.A. Payne, L. Stephens, J. Mauzeroll, The application of scanning electrochemical microscopy to corrosion research, Corrosion 73 (2017) 759–780, https://doi.org/10.5006/2354.
[4] N. Ebejer, A.G. Güell, S.C.S. Lai, K. McKelvey, M.E. Snowden, P.R. Unwin, Scanning electrochemical cell microscopy: a versatile technique for nanoscale electrochemistry and functional imaging, Annu. Rev. Anal. Chem. 6 (2013) 329–351, https://doi.org/10.1146/annurev-anchem-062012-092650.
[5] H. Böhni, T. Suter, A. Schreyer, Micro- and nanotechniques to study localized corrosion, Electrochim. Acta 40 (1995) 1361–1368, https://doi.org/10.1016/0013-4686(95)00072-M.
[6] T. Suter, H. Böhni, A new microelectrochemical method to study pit initiation on stainless steels, Electrochim. Acta 42 (1997) 3275–3280, https://doi.org/10.1016/S0013-4686(70)01783-8.
[7] T. Suter, H. Böhni, Microelectrodes for studies of localized corrosion processes, Electrochim. Acta 43 (1998) 2843–2849, https://doi.org/10.1016/S0013-4686(98)00025-5.
[8] E.G. Webb, R.C. Alkire, Pit initiation at single sulfide inclusions in stainless steel, J. Electrochem. Soc. 149 (2002) B286, https://doi.org/10.1149/1.1474432.
[9] R. a Perren, T. a Suter, P.J. Uggowitzer, L. Weber, R. Magdowski, H. Böhni, M.O. Speidel, Corrosion resistance of super duplex stainless steels in chloride ion containing environments: investigations by means of a new micro-electrochemical method.II. Influence of precipitates, Corros. Sci. 43 (2001) 727–745, https://doi.org/10.1016/S0010-938X(00)00088-3.
[10] C.J. Park, H.S. Kwon, M.M. Lohrengel, Micro-electrochemical polarization study on 25% Cr duplex stainless steel, Mater. Sci. Eng. 372 (2004) 180–185, https://doi.org/10.1016/j.msea.2003.12.013.
[11] V. Vignal, N. Mary, R. Oltra, J. Peultier, A mechanical–electrochemical approach for the determination of precursor sites for pitting corrosion at the microscale, J. Electrochem. Soc. 153 (2006) B352, https://doi.org/10.1149/1.2218762.
[12] F. Andreatta, M.M. Lohrengel, H. Terryn, J.H.W. De Wit, Electrochemical characterisation of aluminium AA7075-T6 and solution heat treated AA7075 using a micro-capillary cell, Electrochim. Acta 48 (2003) 3239–3247, https://doi.org/10.1016/S0013-4686(03)00379-7.
[13] N. Birbilis, R.G. Buchheit, Electrochemical characteristics of intermetallic phases in aluminum alloys, J. Electrochem. Soc. 152 (2005) B140, https://doi.org/10.1149/1.1869984.
[14] A.J. Bard, F.R.F. Fan, J. Kwak, O. Lev, Scanning electrochemical microscopy. Introduction and principles, Anal. Chem. 61 (1989) 132–138, 0003-2700/89/0361-0132$01.50/.
[15] S. Amemiya, A.J. Bard, F.R.F. Fan, M.V. Mirkin, P.R. Unwin, Scanning electrochemical microscopy, Anal. Chem. 1 (2008) 95–131, https://doi.org/10.1149/1.2096429.
[16] Y. Yuan, L. Li, C. Wang, Y. Zhu, Study of the effects of hydrogen on the pitting processes of X70 carbon steel with SECM, Electrochem. Commun. 12 (2010) 1804–1807, https://doi.org/10.1016/j.elecom.2010.10.031.
[17] C.H. Paik, H.S. White, R.C. Alkire, Scanning electrochemical microscopy detection of dissolved sulfur species from inclusions in stainless steel, J. Electrochem. Soc. 147 (2000) 4120, https://doi.org/10.1149/1.1394028.
[18] C.F. Dong, H. Luo, K. Xiao, X.G. Li, Y.F. Cheng, In situ characterization of pitting corrosion of stainless steel by a scanning electrochemical microscopy, J. Mater. Eng. Perform. 21 (2012) 406–410, https://doi.org/10.1007/s11665-011-9899-y.
[19] A.C. Bastos, A.M. Simões, S. González, Y. González-García, R.M. Souto, Imaging concentration profiles of redox-active species in open-circuit corrosion processes with the scanning electrochemical microscope, Electrochem. Commun. 6 (2004) 1212–1215, https://doi.org/10.1016/j.elecom.2004.09.022.
[20] J. Izquierdo, A. Eifert, R.M. Souto, C. Kranz, Simultaneous pit generation and visualization of pit topography using combined atomic force-scanning electrochemical microscopy, Electrochem. Commun. 51 (2015) 15–18, https://doi.org/10.1016/j.elecom.2014.11.017.
[21] N. Casillas, S.J. Charlebois, W.H. Smyrl, H.S. White, Pitting corrosion of titanium, J. Electrochem. Soc. 141 (1994) 636–642, https://doi.org/10.1179/000705972798323297.
[22] C.L. Bentley, M. Kang, P.R. Unwin, Scanning electrochemical cell microscopy: new perspectives on electrode processes in action, Curr. Opin. Electrochem. 6 (2017) 23–30, https://doi.org/10.1016/j.coelec.2017.06.011.
[23] C.L. Bentley, M. Kang, P.R. Unwin, Nanoscale structure dynamics within electrocatalytic materials, J. Am. Chem. Soc. 139 (2017) 16813–16821, https://doi.org/10.1021/jacs.7b09355.
[24] C.L. Bentley, P.R. Unwin, Nanoscale electrochemical movies and synchronous topographical mapping of electrocatalytic materials, Faraday Discuss 210 (2018) 365–379, https://doi.org/10.1039/C8FD00028J.
[25] N. Ebejer, M. Schnippering, A.W. Colburn, M.A. Edwards, P.R. Unwin, Localized high resolution electrochemistry and multifunctional Imaging : scanning electrochemical cell microscopy, Anal. Chem. 82 (2010) 9141–9145, https://doi.org/10.1021/ac102191u.
[26] P.R. Unwin, A.G. Güell, G. Zhang, Nanoscale electrochemistry of sp2 carbon materials: from graphite and graphene to carbon nanotubes, Acc. Chem. Res. 49 (2016) 2041–2048, https://doi.org/10.1021/acs.accounts.6b00301.
[27] C.L. Bentley, M. Kang, F. Maddar, F. Li, M. Walker, J. Zhang, P.R. Unwin, Electrochemical maps and movies of the hydrogen evolution reaction on natural crystals of molybdenite (MoS 2): basal vs. Edge plane activity, Chem. Sci. 8 (2017) 6583–6593, https://doi.org/10.1039/C7SC02545A.
[28] C.L. Bentley, C. Andronescu, M. Smialkowski, M. Kang, T. Tarnev, B. Marler, P.R. Unwin, U.P. Apfel, W. Schuhmann, Local surface structure and composition control the hydrogen evolution reaction on iron nickel sulfides, Angew. Chem. Int. Ed. 57 (2018) 4093–4097, https://doi.org/10.1002/anie.201712679.
[29] D. Lopez, T. Perez, S.N. Simison, The influence of microstructure and chemical composition of carbon and low alloy steels in CO2 corrosion . A state-of-the-art appraisal, Mater. Des. 24 (2003) 561–575, https://doi.org/10.1016/S0261-3069.
[30] J. Guo, S. Yang, C. Shang, Y. Wang, X. He, Influence of carbon content and microstructure on corrosion behaviour of low alloy steels in a Cl- containing environment, Corros. Sci. 51 (2008) 242–251, https://doi.org/10.1016/j.corsci.2008.10.025.
[31] C.L. Bentley, D. Perry, P.R. Unwin, Stability and placement of Ag/AgCl quasi-reference counter electrodes in confined electrochemical cells, Anal. Chem. 90 (2018) 7700–7707, https://doi.org/10.1021/acs.analchem.8b01588.
[32] M.E. Snowden, A.G. Gu, S.C.S. Lai, K.M. Kelvey, N. Ebejer, M.A.O. Connell, A.W. Colburn, P.R. Unwin, Scanning electrochemical cell microscopy: theory and experiment for quantitative high resolution spatially-resolved voltammetry and simultaneous ion-conductance measurements, Anal. Chem. 84 (2012) 2483–2491, https://doi.org/10.1021/ac203195h.
[33] C.H. Chen, L. Jacobse, K. McKelvey, S.C.S. Lai, M.T.M. Koper, P.R. Unwin, Voltammetric scanning electrochemical cell microscopy: dynamic imaging of hydrazine electro-oxidation on platinum electrodes, Anal. Chem. 87 (2015) 5782–5789, https://doi.org/10.1021/acs.analchem.5b00988.
[34] M.M. Lohrengel, A. Moehring, M. Pilaski, Capillary-based droplet cells: limits and new aspects, Electrochim. Acta 47 (2001) 137–141, https://doi.org/10.1016/S0013-4686(01)00570-9.
[35] J. Ustarroz, M. Kang, E. Bullions, P.R. Unwin, Impact and oxidation of single silver nanoparticles at electrode surfaces: one shot versus multiple events, Chem. Sci. 8 (2016) 1841–1853, https://doi.org/10.1039/C6SC04483B.
[36] C.L. Bentley, M. Kang, P.R. Unwin, Time-resolved detection of surface oxide formation at individual gold nanoparticles: role in electrocatalysis and new approach for sizing by electrochemical impacts, J. Am. Chem. Soc. 138 (2016) 12755–12758, https://doi.org/10.1021/jacs.6b08124.
[37] M. Kang, D. Perry, Y.R. Kim, A.W. Colburn, R.A. Lazenby, P.R. Unwin, Time-resolved detection and analysis of single nanoparticle electrocatalytic impacts, J. Am. Chem. Soc. 137 (2015) 10902–10905, https://doi.org/10.1021/jacs.5b05856.
[38] C.H. Chen, E.R. Ravenhill, D. Momotenko, Y.R. Kim, S.C.S. Lai, P.R. Unwin, Impact of surface chemistry on nanoparticle-electrode interactions in the electrochemical detection of nanoparticle collisions, Langmuir 31 (2015) 11932–11942, https://doi.org/10.1021/acs.langmuir.5b03033.
[39] S.E.F. Kleijn, S.C.S. Lai, T.S. Miller, A.I. Yanson, M.T.M. Koper, P.R. Unwin, Landing and catalytic characterization of individual nanoparticles on electrode surfaces, J. Am. Chem. Soc. 134 (2012) 18558–18561, https://doi.org/10.1021/ja309220m.
[40] M. Kang, D. Momotenko, A. Page, D. Perry, P.R. Unwin, Frontiers in nanoscale electrochemical imaging: faster, multifunctional, and ultrasensitive, Langmuir 32 (2016) 7993–8008, https://doi.org/10.1021/acs.langmuir.6b01932.
[41] H. Krawiec, V. Vignal, R. Akid, Numerical modelling of the electrochemical behaviour of 316L stainless steel based upon static and dynamic experimental microcapillary-based techniques, Electrochim. Acta 53 (2008) 5252–5259, https://doi.org/10.1016/j.electacta.2008.02.063.
[42] C.G. Williams, M.A. Edwards, A.L. Colley, J.V. Macpherson, P.R. Unwin, Scanning micropipet contact method for high-resolution imaging of electrode surface redox activity, Anal. Chem. 81 (2009) 2486–2495, https://doi.org/10.1021/ac802114r.
[43] N. Birbilis, B.N. Padgett, R.G. Buchheit, Limitations in microelectrochemical capillary cell testing and transformation of electrochemical transients for acquisition of microcell impedance data, Electrochim. Acta 50 (2005) 3536–3544, https://doi.org/10.1016/j.electacta.2005.01.010.
[44] F. Arjmand, A. Adriaens, Microcapillary electrochemical droplet cells: applications in solid-state surface analysis, J. Solid State Electrochem. 18 (2014) 1779–1788, https://doi.org/10.1007/s10008-014-2413-3.
[45] T. Suter, R.C. Alkire, Microelectrochemical studies of pit initiation at single inclusions in Al 2024-T3, J. Electrochem. Soc. 148 (2001) B36, https://doi.org/10.1149/1.1344530.
[46] X.L. Zhang, Z.H. Jiang, Z.P. Yao, Y. Song, Z.D. Wu, Effects of scan rate on the

potentiodynamic polarization curve obtained to determine the Tafel slopes and corrosion current density, Corros. Sci. 51 (2009) 581–587, https://doi.org/10.1016/j.corsci.2008.12.005.
[47] ASTM G102-89(2015)e1, Standard Practice for Calculation of Corrosion Rates and Related Information from Electrochemical Measurements, West Conshohocken, PA, 2015, https://doi.org/10.1520/G0102-89R15E01.
[48] M. Pourbaix, Atlas of Electrochemical Equilibria in Aqueous Solutions. IV. Establishment and Interpretation of Potential-pH Equilibrium Diagrams, first ed., Pergamon Press, London, 1966.
[49] C.-H. Chen, K.E. Meadows, A. Cuharuc, S.C.S. Lai, P.R. Unwin, High resolution mapping of oxygen reduction reaction kinetics at polycrystalline platinum electrodes, Phys. Chem. Chem. Phys. 16 (2014) 18545, https://doi.org/10.1039/C4CP01511H.
[50] M. Pourbaix, Lectures on Electrochemical Corrosion, first ed., Springer US, 1973 https://doi.org/10.1007/978-1-4684-1806-4.
[51] M.G. Fontana, Corrosion Engineering, third ed., McGraw-Hill Inc, 1986.
[52] A. Schreiber, J.W. Schultze, M.M. Lohrengel, F. Kármán, E. Kálmán, Grain dependent electrochemical investigations on pure iron in acetate buffer pH 6.0, Electrochim. Acta 51 (2006) 2625–2630, https://doi.org/10.1016/j.electacta.2005.07.052.
[53] A. Schreiber, C. Rosenkranz, M.M. Lohrengel, Grain-dependent anodic dissolution of iron, Electrochim. Acta 52 (2007) 7738–7745, https://doi.org/10.1016/j.electacta.2006.12.062.
[54] M. Seo, M. Chiba, Nano-mechano-electrochemistry of passive metal surfaces, Electrochim. Acta 47 (2001) 319–325, https://doi.org/10.1016/S0013-4686(01)00577-1.
[55] M. Chiba, M. Seo, Mechanoelectrochemical properties of passive iron surfaces evaluated by an in situ nanoscratching test, J. Electrochem. Soc. 150 (2003) B525, https://doi.org/10.1149/1.1615994.
[56] V. Rault, V. Vignal, H. Krawiec, F. Dufour, Quantitative assessment of local misorientations and pitting corrosion behaviour of pearlitic steel using electron backscattered diffraction and microcapillary techniques, Corros. Sci. 100 (2015) 667–671, https://doi.org/10.1016/j.corsci.2015.08.002.
[57] K.A. Lill, A.W. Hassel, G. Frommeyer, M. Stratmann, Scanning droplet cell investigations on single grains of a FeAlCr light weight ferritic steel, Electrochim. Acta 51 (2005) 978–983, https://doi.org/10.1016/j.electacta.2005.05.068.
[58] A. Shahryari, J.A. Szpunar, S. Omanovic, The influence of crystallographic orientation distribution on 316LVM stainless steel pitting behavior, Corros. Sci. 51 (2009) 677–682, https://doi.org/10.1016/j.corsci.2008.12.019.
[59] H. Krawiec, Z. Szklarz, Combining the Electrochemical Microcell Technique and the Electron Backscatter Diffraction method to study the electrochemical behaviour of polycrystalline aluminium in sodium chloride solution, Electrochim. Acta 203 (2016) 426–438, https://doi.org/10.1016/j.electacta.2016.03.030.
[60] B.D.B. Aaronson, C.H. Chen, H. Li, M.T.M. Koper, S.C.S. Lai, P.R. Unwin, Pseudo-single-crystal electrochemistry on polycrystalline electrodes: visualizing activity at grains and grain boundaries on platinum for the Fe 2+/Fe3+ redox reaction, J. Am. Chem. Soc. 135 (2013) 3873–3880, https://doi.org/10.1021/ja310632k.
[61] K. Fushimi, M. Seo, An SECM observation of dissolution distribution of ferrous or ferric ion from a polycrystalline iron electrode, Electrochim. Acta 47 (2001) 121–127, https://doi.org/10.1016/S0013-4686(01)00557-6.
[62] A.J. Davenport, L.J. Oblonsky, M.P. Ryan, M.F. Toney, The structure of the passive film that forms on iron in aqueous environments, J. Electrochem. Soc. 147 (2000) 2162–2173, https://doi.org/10.1149/1.1393502.
[63] D. Dwivedi, K. Lepková, T. Becker, Carbon steel corrosion: a review of key surface properties and characterization methods, RSC Adv. 7 (2017) 4580–4610, https://doi.org/10.1039/C6RA25094G.
[64] G.S. Eklund, Initiation of pitting at sulfide inclusions in stainless steel, J. Electrochem. Soc. 121 (1974) 467, https://doi.org/10.1149/1.2401840.
[65] G. Wranglen, Pitting and sulphide inclusions in steel, Corros. Sci. 14 (1974) 331–349, https://doi.org/10.1016/S0010-938X(74)80047-8.
[66] E.G. Webb, T. Suter, R.C. Alkire, Microelectrochemical measurements of the dissolution of single MnS inclusions, and the prediction of the critical conditions for pit initiation on stainless steel, J. Electrochem. Soc. 148 (2001) B186–B195, https://doi.org/10.1149/1.1360205.